Evolution and Physical Characteristics of a Raceway Based on a Transient Eulerian Multiphase Flow Model

Authors:

Xing Peng, Jingsong Wang, Haibin Zuo, Qingguo Xue

Abstract:

In industrial processes, a semi-cavity area formed by airflow wherein the particles circulate is called a "raceway". In a blast furnace, the role of the raceway is particularly important. To understand and predict the evolution and physical characteristics of the raceway, a three-dimensional transient Eulerian multiphase flow model in a packed particle bed was developed. In the model, it was assumed that the gas and solid (particle) phases constitute an interpenetrating continuum. The gas-phase turbulence was described as a k?? dispersed model. The gas-phase stress was considered in terms of the effective viscosity of the gas. The solid-phase constitutive relationship was expressed in terms of solid stress. It was found that the evolution process of the raceway can be divided into three stages: (1) rapid expansion, (2) slow contraction, and (3) gradual stabilization. When the blast velocity was increased from 150 m/s to 300 m/s, the surface area of the raceway increased from 0.194 m2 to 1.644 m2. The depth and height of the raceway increased considerably with velocity, while the width slightly increased.

Evolution and Physical Characteristics of a Raceway Based on a Transient Eulerian Multiphase Flow Model

Xing Peng, Jingsong Wang *, Haibin Zuo and Qingguo Xue

State Key Laboratory of Advanced Metallurgy, University of Science and Technology Beijing, Beijing 100083, China; pengxing_hunan@sina.com (X.P.); zuohaibin@ustb.edu.cn (H.Z.); xueqingguo@ustb.edu.cn (Q.X.)

* Correspondence: wangjingsong@ustb.edu.cn; Tel.: +86-010-82375181

Abstract: In industrial processes, a semi-cavity area formed by airflow wherein the particles circulate is called a "raceway". In a blast furnace, the role of the raceway is particularly important. To understand and predict the evolution and physical characteristics of the raceway, a three-dimensional transient Eulerian multiphase flow model in a packed particle bed was developed. In the model, it was assumed that the gas and solid (particle) phases constitute an interpenetrating continuum. The gas-phase turbulence was described as a k–ε dispersed model. The gas-phase stress was considered in terms of the effective viscosity of the gas. The solid-phase constitutive relationship was expressed in terms of solid stress. It was found that the evolution process of the raceway can be divided into three stages: (1) rapid expansion, (2) slow contraction, and (3) gradual stabilization. When the blast velocity was increased from 150 m/s to 300 m/s, the surface area of the raceway increased from 0.194 m^2 to 1.644 m^2. The depth and height of the raceway increased considerably with velocity, while the width slightly increased.

1. Introduction

In a blast furnace (BF), the raceway is formed by airflow wherein the particles circulate. The combustion of coke and injected fuels in the raceway supplies gas and heat for the critical endothermic reduction of iron ores and for iron smelting [1]. Therefore, the raceway characteristics directly affect the primary distribution of gas and heat inside the BF. Some previous studies have used empirical size characteristics of the raceway to predict the combustion of pulverized coal and the gas flow distribution, which may considerably differ from those of the actual BF raceway [2–4]. The raceway depth directly affects the burnout rate of pulverized coal and determines the airflow distribution in the center of the blast furnace. The flow pattern will determine the strength of gas–solid mixing and the rate of coke consumption, thereby further affecting the smelting efficiency of the blast furnace. Therefore, it is necessary to understand the evolution process and physical characteristics of the raceway.

Investigations of the BF raceway phenomenon and its characteristics can be carried out via three methods: theoretical analysis, experimental testing, and numerical modeling. In theoretical analyses, some studies analyzed the raceway size on the basis of the force balance of the raceway boundary in different spatial dimensions [5–8]. The phenomenon of raceway hysteresis was explained, together with the effects of chemical reactions, blast velocity, material layer porosity, particle diameter, and other factors. However, this method treats the raceway as a circle or a sphere and disregards the force between the particles. Thus, it can be considered a relatively inaccurate method.

In experimental testing, the microwave reflection method was used to study the formation and depth of the BF raceway during production [9]. The effects of tuyere diameter, air volume, and coal

injection on the depth of the raceway zone were investigated. In contrast, considering that the complex environment, in terms of high temperature and pressure in the raceway, implies significant difficulties for direct research, most researchers used cold models to study the formation and physical characteristics of the raceway [10–16]. However, it was challenging for the researchers to experimentally obtain dynamic information and accurately measure the raceway characteristics in three-dimensional (3D) space through experimental testing.

With the advancement of computers, numerical modeling has become a more popular method. A combined computational fluid dynamics and discrete element method (CFD-DEM) was developed [17–23]. The effects of different variables on the raceway were investigated. Nonetheless, previous CFD-DEM-based studies generally used two-dimensional (2D) or pseudo 3D models and small sizes with certain divergences from actual conditions. Hilton et al. [24] and Lichtenegger et al. [25] used the CFD-DEM method to investigate the effect of particle properties on the evolution of the raceway in 3D packed beds. However, these previously reported approaches were computationally expensive. Also, these approaches did not facilitate quantitative analysis of the raceway or the investigation of raceway physical characteristics.

However, the gas–solid flow model based on CFD can achieve high efficiency at low computational cost. The shape and size of the raceway was studied in a 2D state using a transient or steady model based on CFD [26–28]. Rangarajan et al. [29] extensively studied the influence of the operating conditions on raceway properties using a two-fluid model. Based on CFD modeling technology, research on coupling fuel combustion and raceway formation has been carried out, and a lot of information about combustion and gas distribution has been obtained [30–36]. However, no details on constitutive relations, the surface area of the raceway, or the evolution of the raceway penetration depth in a short time interval can be found in these articles.

In this study, we developed an industrial-scale blast furnace 3D slot model based on a transient Eulerian multiphase flow model (EMFM). The influence of the chemical reaction in the BF on the raceway characteristics is mainly reflected in the change in gas flow [26]. For simplicity, we did not set the combustion reaction or heat transfer, but we set the initial bed solid packing fraction to be less than the maximum volume fraction as an approximate replacement. The evolution process and flow pattern of the raceway are revealed. The depth, height, width, and surface area of the raceway were predicted, providing detailed information and theoretical guidance for the process of gas injection into packed beds in industrial processes.

2. Model Description

The model assumes that the gas phase and the solid (particle) phase constitute an interpenetrating continuum. The different phases appear in the same calculated cell and are characterized by the volume fraction, α_i, of each phase i (gas, solid). The gas-phase turbulence was described as a k–ε dispersed model and the gas-phase stress was considered in terms of effective viscosity. An advanced constitutive relation was adopted to describe solid stress.

2.1. Conservation Equations

In the process of gas–solid flow, both the gas and particle flows satisfy the conservation of mass and momentum. Given that there is no mass exchange between the solid particles and the gas phase, they are independent of each other. The mass conservation equation for phase i can be expressed as

$$\frac{\partial(\alpha_i \rho_i)}{\partial t} + \nabla \cdot (\alpha_i \rho_i U_i) = 0, \tag{1}$$

$$\Sigma \alpha_i = 1. \tag{2}$$

The momentum conservation equation for phase i can be written as

$$\frac{\partial(\alpha_i\rho_iU_i)}{\partial t} + \nabla\cdot(\alpha_i\rho_iU_iU_i) = \nabla\cdot\tau_i + \alpha_i\rho_ig + S. \tag{3}$$

The source term, S, is generated by the momentum transfer between the gas and solid phases and is expressed as

$$S = \beta\left(U_j - U_i\right),\ j \neq i. \tag{4}$$

For $\alpha_g > 0.8$, coefficient β is based on the drag force of the fluid acting on a single particle, and for $\alpha_g \leq 0.8$, β is described by Ergun's equation [37]. Thus, β can be expressed as

$$\beta = \begin{cases} \frac{3}{4}C_D\frac{\alpha_s\alpha_g\rho_g|U_s-U_g|}{d_s}\alpha_g^{-2.65} & \alpha_g > 0.8 \\ 150\frac{\alpha_s^2\mu_g}{\alpha_gd_s^2} + 1.75\frac{P_g\alpha_s|U_s-U_g|}{d_s} & \alpha_g \leq 0.8 \end{cases} \tag{5}$$

where d_s is the solid (particle) diameter; the drag coefficient, C_D, is given by

$$C_D = \begin{cases} \frac{24}{\alpha_gRe}\left[1+0.15\left(\alpha_gRe\right)^{0.687}\right] & Re \leq 1000 \\ 0.44 & Re > 1000 \end{cases} \tag{6}$$

where Re is the particle Reynolds number and can be expressed as

$$Re = \frac{\rho_gd_s|U_s-U_g|}{\mu_g}. \tag{7}$$

2.2. Constitutive Relations

The gas-phase constitutive equation is characterized by the effective viscosity of the gas. The solid-phase constitutive relationship is expressed in terms of solid stress. Tables 1 and 2 summarize a detailed description of the constitutive relations [37–42].

Table 1. Gas constitutive relations.

Item	Formula
Gas stress	$\tau_g = -P_gI + \mu_{eff,g}(\nabla U_g + (\nabla U_g)^T) - \frac{2}{3}\left(\mu_{eff,g}\left(\nabla\cdot U_g\right)I + \rho_gk_g\right)$
Gas effective viscosity	$\mu_{eff,g} = \mu_g + \mu_{t,g}$
Gas turbulent viscosity	$\mu_{t,g} = \rho_gC_\mu\frac{k_g^2}{\varepsilon_g}$ $(C_\mu = 0.09)$

Table 2. Solid constitutive relations.

Item	Formula
Solid stress	$\tau_s = (-P_s + \xi_s\nabla\cdot U_s)I + \mu_s\left\{\left(\nabla U_s + \nabla U_s^T\right) - \frac{2}{3}\nabla U_sI\right\}$
Solid pressure	$P_s = \alpha_s\rho_s\Theta + 2\rho_s(1+e)\alpha_s^2g_0\Theta$
Diffusion coefficient	$k_s = \frac{150\rho_sd_s\sqrt{\Theta\pi}}{384(1+e)g_0}\left[1 + \frac{6}{5}g_0\alpha_s(1+e)\right]^2 + 2\alpha_s^2\rho_sd_sg_0(1+e)(\frac{\Theta}{\pi})^{1/2}$
Particle collisional dissipation of energy	$\gamma_s = 3\left(1-e^2\right)g_0\rho_s\alpha_s^2\Theta(\frac{4}{d_s}(\frac{\Theta}{\pi})^{1/2} - \nabla\cdot U_s)$
Solid radial distribution function	$g_0 = \frac{3}{5}\left[1-[\frac{\alpha_s}{\alpha_{s,\ max}}]^{1/3}\right]^{-1}$
Solid bulk viscosity	$\xi_s = \frac{4}{3}\alpha_s^2\rho_sd_sg_0(1+e)(\frac{\Theta}{\pi})^{1/2}$
Solids shear viscosity	$\mu_s = \mu_{s,kin} + \mu_{s,col} + \mu_{s,fr}$
Solid kinetic viscosity	$\mu_{s,kin} = \frac{10\rho_sd_s\sqrt{\Theta\pi}}{96(1+e)g_0}\left[1 + \frac{4}{5}g_0\alpha_s(1+e)\right]^2$
Solid collisional viscosity	$\mu_{s,col} = \frac{4}{5}\alpha_s^2\rho_sd_sg_0(1+e)(\frac{\Theta}{\pi})^{1/2}$
Solid frictional viscosity	$\mu_{s,fr} = \frac{P_{friction}\ \sin\phi}{2\ \sqrt{I_{2D}}}$
Frictional pressure	$P_{friction} = \begin{cases} Fr\frac{(\alpha_s-\alpha_{s,min})^2}{(\alpha_{s,max}-\alpha_s)^5},Fr = 0.1\alpha_s,\ \alpha_s \geq 0.5 \\ 0 \qquad\qquad\qquad \alpha_s < 0.5 \end{cases}$

2.3. Turbulence Equations

Turbulence predictions were obtained from a k–ε dispersed model. The transport equations were expressed as follows:

$$\frac{\partial}{\partial t}\left(\alpha_g \rho_g k_g\right) + \nabla \cdot \left(\alpha_g \rho_g U_g k_g\right) = \nabla \cdot \left(\alpha_g \frac{\mu_{t,g}}{\sigma_k} \nabla k_g\right) + \alpha_g G_{k,g} - \alpha_g \rho_g \varepsilon_g + \alpha_g \rho_g \Pi_{k_g} \tag{8}$$

$$\frac{\partial}{\partial t}\left(\alpha_g \rho_g \varepsilon_g\right) + \nabla \cdot \left(\alpha_g \rho_g U_g \varepsilon_g\right) = \nabla \cdot \left(\alpha_g \frac{\mu_{t,g}}{\sigma_\varepsilon} \nabla \varepsilon_g\right) + \alpha_g \frac{\varepsilon_g}{k_g}\left(C_{1\varepsilon} G_{k,g} - C_{2\varepsilon} \rho_g \varepsilon_g\right) + \alpha_g \rho_g \Pi_{\varepsilon_g} \tag{9}$$

where Π_{k_g} and Π_{ε_g} are source terms that can be included to model the influence of the dispersed phases on the continuous phase. The constants for the k–ε model were taken as $\sigma_k = 1.00$, $\sigma_\varepsilon = 1.30$, $C_{1\varepsilon} = 1.44$, and $C_{2\varepsilon} = 1.92$ [26].

2.4. Geometry and Operating Conditions

To save computing resources, a slot model of the lower part of the BF was derived. Figure 1 depicts the computational domain. The geometric model covers the iron slag surface to the furnace bosh, with the deadman removed. Its size is based on a small steel plant BF. The EMFM equations were calculated using ANSYS–FLUENT 17.2. The phase-coupled SIMPLE (PC-SIMPLE) algorithm was used for the coupling between pressure and velocity. The second-order upwind style was used in the discretization scheme.
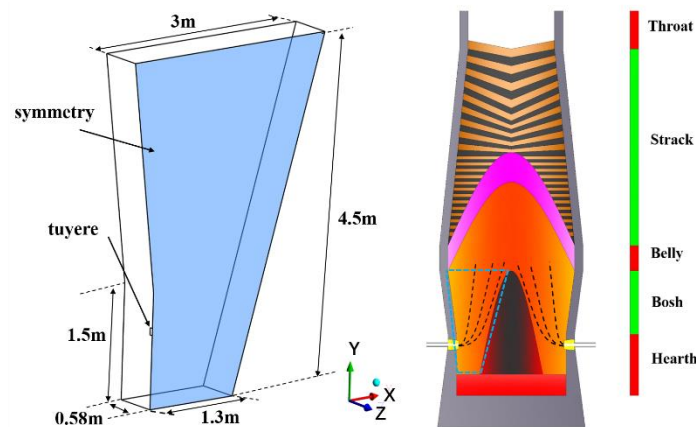

Figure 1. Blast furnace (BF) schematic and geometry model of the calculation domain.

Tables 3 and 4 list the simulation parameters and computational conditions, respectively. Injection angles of 5° were associated with the negative direction of the *y* axis. The chemical reaction, the polydispersity of the particles, and the liquid phase were not considered during the flow process. Therefore, to replace the effects of the above factors, and in combination with the actual charge void distribution in the lower part of the BF, the solid volume fraction was set to 0.6, which is less than the maximum limiting volume fraction ($\alpha_{s,max}$). Considering the pressure of the upper layer of the BF, the outlet pressure was set to 303,000 Pa.

Table 3. Simulation parameters.

Parameters	Value
Number of calculation units	109,516
Time Step	0.0001 s
Particle density	1000 kg/m^3
Angle of internal friction	30°
Tuyere equivalent diameter	0.113 m
Initial solid volume fraction	0.6
Solid packing limit	0.7
Friction packing limit	0.61
Initial bed particle height	4 m
Outlet pressure	303,000 Pa

Table 4. Computational conditions.

Case	Blast Velocity (m/s)	Injection Angle	Particle Diameter (m)
1	150	5°	0.01
2	200	5°	0.01
3	250	5°	0.01
4	300	5°	0.01

2.5. Grid and Time Step Independence

Table 5 shows the raceway size after stabilization under different grids and time steps. Further refinement of the grid in either direction did not change the raceway size by more than 2%, which verifies the independence of the computational domain grid. The simulation result did not change by more than 1% by further reducing the time step. This demonstrates the reliability of the numerical model.

Table 5. Raceway size of different numbers of grid cells and time steps.

Number of Grid Cells	Time Step (s)	Depth (mm)	Height (mm)	Width (mm)	Deviation
109,516	0.0001	631	458	264	-
300,672	0.0001	640	461	267	<2%
109,516	0.00005	637	462	266	<1%

3. Results and Discussion

3.1. Raceway Evolution Characteristics

Raceway evolution is an important phenomenon, particularly reblowing, which occurs after a temporary wind break in an ironmaking BF. To accurately analyze the evolution process and physical characteristics of the raceway, the boundary of the raceway was previously defined by the values of isostatic stress and solid or gas volume fractions [24–27]. In this study, when the solid volume fraction was less than 0.5, the frictional pressure was 0, and the solid motion was mainly affected by collision. Therefore, the boundary of the raceway was defined as a solid volume fraction of 0.5.

As depicted in Figure 2, at an injection velocity of 150 m/s, the penetration depth of the raceway reached a peak at 1 s, at a value of 0.783 m, and it stabilized at 9 s, at a value of 0.386 m. At an injection velocity of 200 m/s, the penetration depth reached 0.982 m at 1.1 s and then decreased to 0.460 m at 25 s. At 250 m/s, the penetration depth increased to a peak of 1.143 m at 1.5 s and achieved a stable value of 0.631 m at 40 s. At 300 m/s, the penetration depth reached a peak of 1.327 m at 1.7 s and stabilized at 1.109 m at 47.5 s. The evolution process of the raceway can be divided into three stages: (1) rapid expansion, (2) slow contraction, and (3) gradual stabilization. In Stage 1, the penetration depth of the raceway increases rapidly in the early stages of gas injection. The higher the injection velocity, the faster

the increase in the penetration depth. Then, in Stage 2, as the particles descend and congregate, the penetration depth decreases slowly after reaching the peak. In Stage 3, the raceway stabilizes.
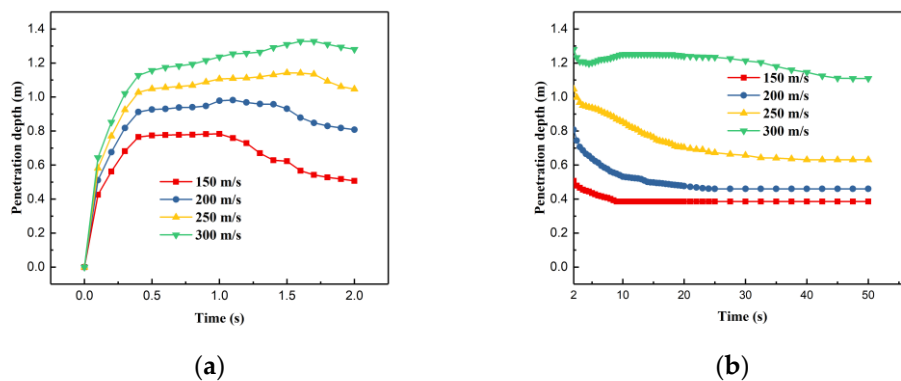

Figure 2. Evolution of penetration depth in the raceway: (**a**) 0–2 s and (**b**) 2–50 s.

A typical blast velocity is close to 250 m/s in a small BF tuyere. Figure 3 depicts the evolution of the raceway. When air was injected through the tuyere, the expansion of the depth of the raceway was more obvious. When the peak was reached, the height changes of the raceway were more obvious. Finally, the raceway stabilized at 40 s. This trend was due to the fact that when the solid phase interacted with the gas phase, the initial solid volume fraction changed toward the maximum limiting volume fraction and eventually stabilized. This created a particle circulation zone attributed to the balance between the drag of the blast and the gravity and pressure of the particles.
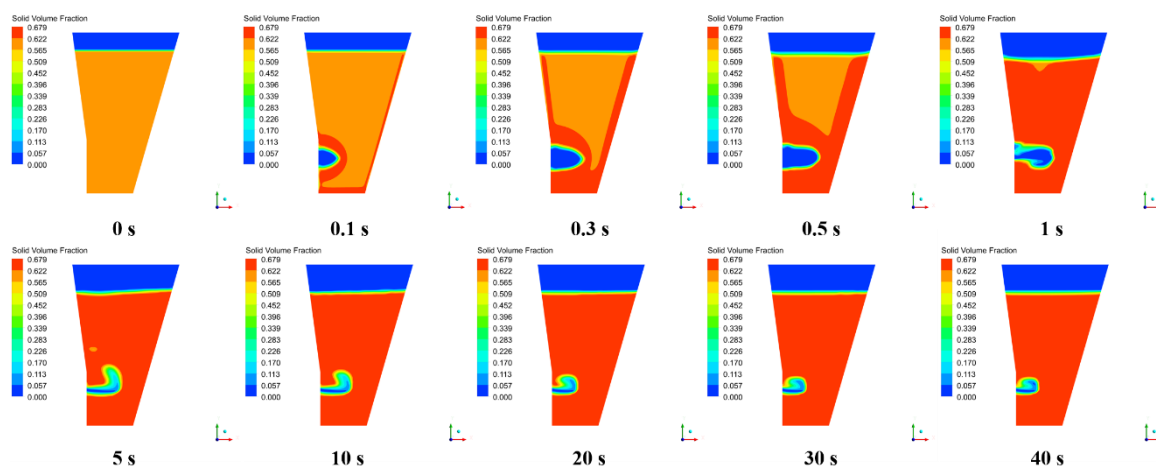

Figure 3. Time evolution of the solid volume fraction for Case 3.

3.2. Raceway Size Characteristics

Different BF operating conditions led to different raceway physical characteristics, which were mainly reflected by their size. Figure 4 shows that the shape of the raceway after it stabilizes is an upturned bag at high blast velocity. In an actual BF, this provides enough space for the combustion of pulverized coal and coke, thereby improving production efficiency.
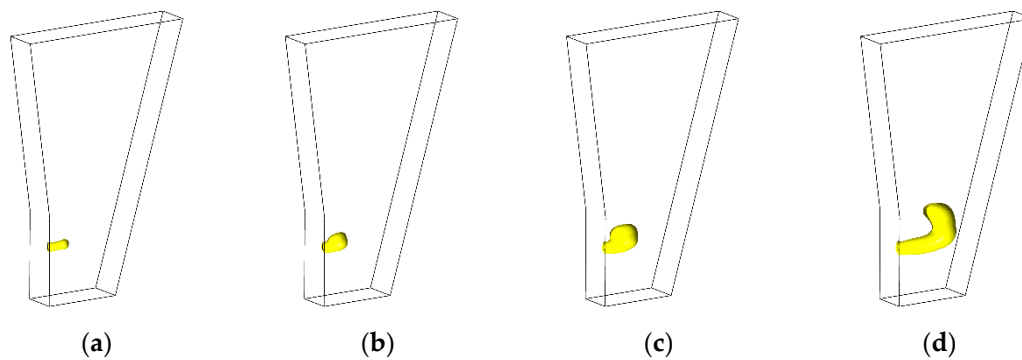
Figure 4. Raceway shapes after they stabilize at different blast velocities: (**a**) 150 m/s; (**b**) 200 m/s; (**c**) 250 m/s; (**d**) 300 m/s.

The blast velocity increase was obviously beneficial for increasing the depth, height, and surface area of the raceway, while the width was slightly increased, as depicted in Figure 5. The size of the raceway was not linearly related to the blast velocity. When the blast velocity was increased from 150 m/s to 300 m/s, the surface area of the raceway increased from 0.194 m^2 to 1.644 m^2, and the depth increased from 0.386 m to 1.109 m. This was due to the increased gas kinetic energy because of the increased blast volume and velocity. Therefore, increasing the blast velocity is very effective for increasing the depth of the raceway in order to develop the central gas flow in an actual BF.
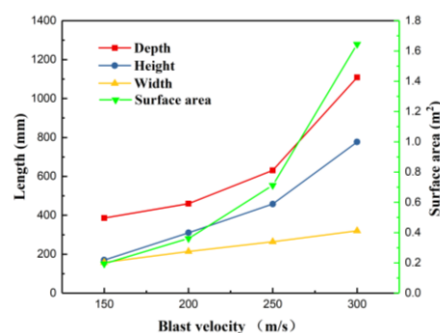

Figure 5. Effect of blast velocity on the raceway size.

3.3. Pressure Distribution

Figure 6a shows that the gas pressure was high in the raceway and decreased as it approached the outlet of the particle bed. In contrast, the solid granular pressure was considerably low in the raceway and at the boundary of the raceway. It is noteworthy that the solid granular pressure reached a local peak at the boundary of the raceway, where gas injection resistance was the highest, as depicted in Figure 6b.

As demonstrated in Figure 7, the gas pressure remained relatively stable up to 0.4 m from the front end of the tuyere because there were fewer particles and low resistance. At a distance equal to or greater than 0.4 m, the air pressure rapidly increased because the gas was subjected to increased particle resistance after deep penetration into the particle bed, and the pressure decreased because the gas velocity decreased and there was further particle resistance. The solid granular pressure in the raceway is close to 0. Near the boundary of the raceway, due to the interaction gas and solid, the solid granular pressure changes drastically, increasing first and then decreasing. However, it slowly increases in the end because the solid were constricted by the wall.
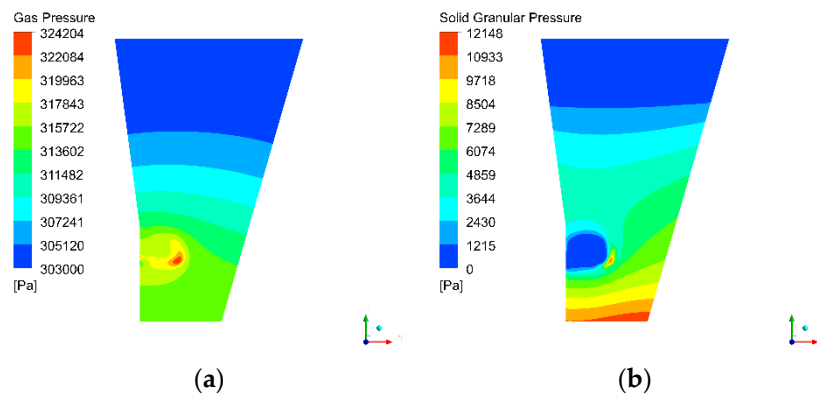
Figure 6. (**a**) Gas pressure and (**b**) solid granular pressure for Case 3 in the symmetry plane at 40 s.
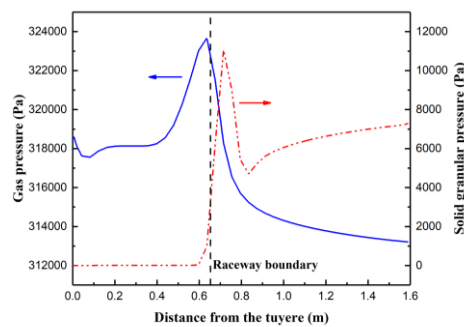

Figure 7. Gas pressure and solid granular pressure for Case 3 on the axis of the tuyere at 40 s.

3.4. Flow Pattern

As depicted in Figures 8a and 9a, the gas in the raceway can be divided into a jet zone and an anti-clockwise flow zone. However, the gas flowed into the particle bed from the boundary of the raceway and did not form a large circulation area. This was due to the injection of high-speed gas into the tuyere, which limited gas circulation in the jet zone. Additionally, the gas had a weak anti-clockwise circulation flow at the edge of the tuyere. This is inconsistent with previous results in which the gas studied according to the CFD-DEM model was divided into anti-clockwise or clockwise circulation or a plume-like flow [21].
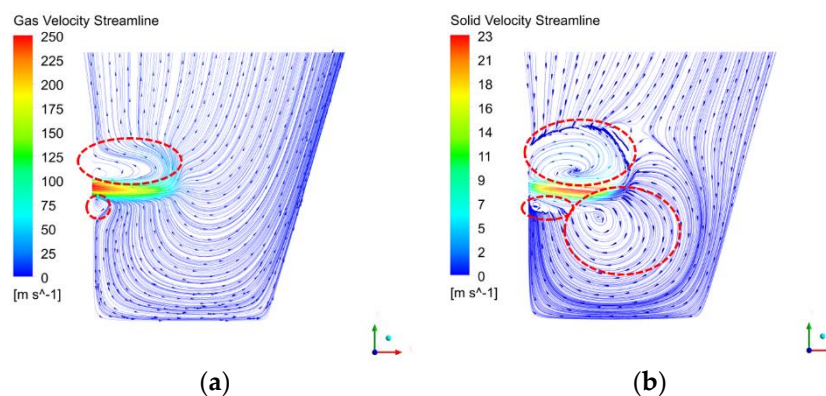

Figure 8. The symmetry plane of Case 3 at 40 s: (**a**) gas velocity streamline; (**b**) solid velocity streamline.
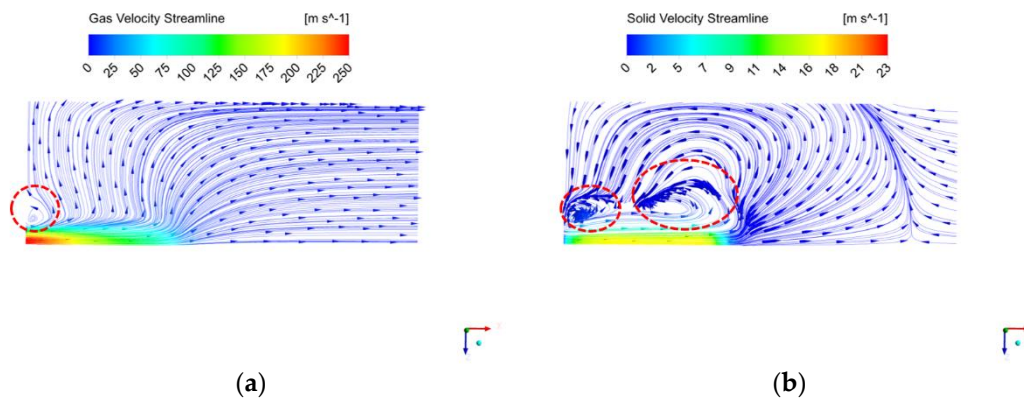
Figure 9. The tuyere level plane of Case 3 at 40 s: (**a**) gas velocity streamline; (**b**) solid velocity streamline.

The particles were clearly circulating anti-clockwise in the raceway, as depicted in Figure 8b. This was mainly due to the higher resistance of the solid particles along the axis of the tuyere and the lower pressure on the upper part of the particle bed. Below the tuyere, two clockwise particle circulation zones were formed, but the movement speed was considerably low. This was because the gas was affected by the solid resistance and the forces on the bottom and the wall. This reduced the gas flow velocity in the lower part of the packed bed, resulting in lower resistance. The source of particles in the solid jet area mainly derived from the upper part of the raceway particles, which also caused the upper particles in the particle bed to move downwards. In the horizontal direction, although there were also two anti-clockwise circulating flows to provide particles for the raceway, as depicted in Figure 9b, their velocities were extremely low. Therefore, the BF raceway was not a single-cycle flow as previously reported [21], but an extremely complex multi-cycle flow with gas–solid interaction. The circulation pattern near the tuyere may have a negative impact on the life of the tuyere.

The gas was injected from the tuyere along the axial direction of the tuyere. Owing to the resistance of the solid particles, the gas velocity rapidly decreased until it reached a value of 0.443 m/s at the wall surface, as depicted in Figure 10. The drag of the gas affected the particles. The particle velocity increased rapidly and maintained a relatively stable value in the middle part of the raceway. However, near the boundary of the raceway ($\alpha_s \rightarrow 0.5$), the particle collision viscosity increased because of the increased particle volume fraction, which considerably reduced the particle velocity. External to the raceway boundary and with an increase in the particle friction viscosity and a decrease in the gas drag, the particle velocity was reduced to a value close to 0.
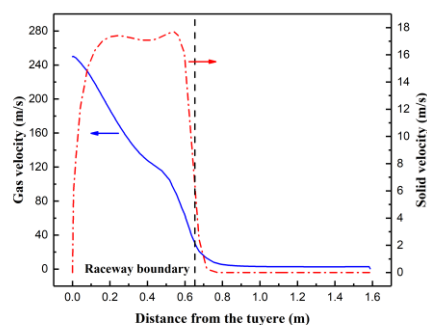

Figure 10. Gas and solid velocity along the axis of the tuyere for Case 3 at 40 s.

4. Conclusions

A 3D transient EMFM was developed to study the evolution and physical characteristics of the raceway in the packed particle bed of an ironmaking BF. The constitutive relation of the gas and solid phases was comprehensively considered in the model. The main conclusions of this study are as follows:

(1)　The evolution process of the raceway can be divided into three stages: rapid expansion, slow contraction, and gradual stabilization. The shape of the raceway was that of an upturned bag at high blast velocity.

(2)　The blast velocity had a significant effect on the size of the raceway. As the velocity increased, the depth, height, and surface area of the raceway considerably increased, while the width slightly increased.

(3)　The gas pressure in the raceway was higher than that of the particle bed, while the solid granular pressure was lower. The raceway did not exhibit a single-cycle flow pattern, but exhibited a complex multiphase and multi-cycle flow pattern.

Notation

Symbol	Meaning
α_i	i phase volume fraction
ρ_i	i phase density, kg/m^3
U_i	i phase velocity, m/s
τ_i	i phase stress–strain tensor, Pa
P_i	i phase pressure, Pa
g	Gravity acceleration, m/s^2
S	Source term
β	Momentum exchange coefficient
C_D	Drag coefficient
d_s	Solid-phase diameter, m
μ_g	Gas-phase viscosity, Pa·s
Re	Reynolds number
I	Unit stress tensor
$\mu_{eff,g}$	Gas effective viscosity, Pa·s
k_g	Gas turbulent kinetic energy, Pa·s
$\mu_{t,g}$	Gas turbulent viscosity, Pa·s
ε_g	Gas turbulent dissipation rate
g_0	Solid radial distribution function
e	Coefficient of restitution for particle collisions
Θ	Granular pseudo-temperature
k_s	Diffusion coefficient
γ_s	Particle collisional dissipation of energy
$\alpha_{s,min}$	Friction packing limit
$\alpha_{s,\,max}$	Packing limit
ξ_s	Solid bulk viscosity, Pa·s
μ_s	Solids shear viscosity, Pa·s
$\mu_{s,kin}$	Solid kinetic viscosity, Pa·s
$\mu_{s,col}$	Solid collisional viscosity, Pa·s
$\mu_{s,fr}$	Solid frictional viscosity, Pa·s
$P_{friction}$	Frictional pressure, Pa

ϕ	Angle of internal friction
I_{2D}	Second invariant of the deviatoric stress tensor
Fr	Froude number
$G_{k,g}$	Gas-phase turbulent kinetic energy
Π_{k_g}	Turbulent kinetic energy source term
Π_{ε_g}	Turbulent dissipation rate source term

References

1. Burgess, J.M. Fuel combustion in the blast furnace raceway zone. *Prog. Energy Combust. Sci.* **1985**, *11*, 61–82. [CrossRef]

2. Zhou, Z.; Xue, Q.; Li, C.; Wang, G.; She, X.; Wang, J. Coal flow and combustion characteristics under oxygen enrichment way of oxygen-coal double lance. *Appl. Therm. Eng.* **2017**, *123*, 1096–1105. [CrossRef]

3. Liu, Y.; Shen, Y. Three-dimensional modelling of charcoal combustion in an industrial scale blast furnace. *Fuel* **2019**, *258*, 116088. [CrossRef]

4. Zhou, Z.; Yi, Q.; Wang, R.; Wang, G.; Ma, C. Numerical investigation on coal combustion in ultralow CO_2 blast furnace: Effect of oxygen temperature. *Processes* **2020**, *8*, 877. [CrossRef]

5. Gupta, G.S.; Rajneesh, S.; Rudolph, V.; Singh, V.; Sarkar, S.; Litster, J.D. Mechanics of raceway hysteresis in a packed bed. *Metall. Mater. Trans. B Process Metall. Mater. Process. Sci.* **2005**, *36*, 755–764. [CrossRef]

6. Gupta, G.S.; Rudolph, V. Comparison of blast furnace raceway size with theory. *ISIJ Int.* **2006**, *46*, 195–201. [CrossRef]

7. Guo, J.; Cheng, S.; Zhao, H.; Pan, H.; Du, P.; Teng, Z. A mechanism model for raceway formation and variation in a blast furnace. *Metall. Mater. Trans. B Process Metall. Mater. Process. Sci.* **2013**, *44*, 487–494. [CrossRef]

8. Li, Y.L.; Cheng, S.S.; Zhang, P.; Guo, J. Development of 3-D mathematical model of raceway size in blast furnace. *Ironmak. Steelmak.* **2016**, *43*, 308–315. [CrossRef]

9. Matsui, Y.; Yamaguchi, Y.; Sawayama, M.; Kitano, S.; Nagai, N.; Imai, T. Analyses on blast furnace raceway formation by micro wave reflection gunned through tuyere. *ISIJ Int.* **2005**, *45*, 1432–1438. [CrossRef]

10. Flint, P.J.; Burgess, J.M. A fundamental study of raceway size in two dimensions. *Metall. Trans. B* **1992**, *23*, 267–283. [CrossRef]

11. Sarkar, S.; Gupta, G.S.; Litster, J.D.; Rudolph, V.; White, E.T.; Choudhary, S.K. A cold model study of raceway hysteresis. *Metall. Mater. Trans. B Process Metall. Mater. Process. Sci.* **2003**, *34*, 183–191. [CrossRef]

12. Sastry, G.S.S.R.K.; Gupta, G.S.; Lahiri, A.K. Cold model study of raceway under mixed particle conditions. *Ironmak. Steelmak.* **2003**, *30*, 61–65. [CrossRef]

13. Sastry, G.S.S.R.K.; Gupta, G.S.; Lahiri, A.K. Void formation and breaking in a packed bed. *ISIJ Int.* **2003**, *43*, 153–160. [CrossRef]

14. Rajneesh, S.; Sarkar, S.; Gupta, G.S. Prediction of raceway size in blast furnace from two dimensional experimental correlations. *ISIJ Int.* **2004**, *44*, 1298–1307. [CrossRef]

15. Mojamdar, V.; Gupta, G.S.; Puthukkudi, A. Raceway formation in a moving bed. *ISIJ Int.* **2018**, *58*, 1396–1401. [CrossRef]

16. Lu, Y.; Jiang, Z.; Zhang, X.; Liu, S.; Wang, J.; Zhang, X. Determination of void boundary in a packed bed by laser attenuation measurement. *Particuology* **2020**, *51*, 72–79. [CrossRef]

17. Xu, B.H.; Yu, A.B.; Chew, S.J.; Zulli, P. Numerical simulation of the gas-solid flow in a bed with lateral gas blasting. *Powder Technol.* **2000**, *109*, 13–26. [CrossRef]

18. Feng, Y.-Q.; Pinson, D.; Yu, A.-B.; Chew, S.J.; Zulli, P. Numerical Study of Gas-Solid Flow in the Raceway of a Blast Furnace. *Steel Res. Int.* **2003**, *74*, 523–530. [CrossRef]

19. Umekage, T.; Yuu, S.; Kadowaki, M. Numerical simulation of blast furnace raceway depth and height, and effect of wall cohesive matter on gas and coke particle flows. *ISIJ Int.* **2005**, *45*, 1416–1425. [CrossRef]

20. Sarkar, S.; Gupta, G.S.; Kitamura, S.Y. Prediction of raceway shape and size. *ISIJ Int.* **2007**, *47*, 1738–1744. [CrossRef]

21. Miao, Z.; Zhou, Z.; Yu, A.B.; Shen, Y. CFD-DEM simulation of raceway formation in an ironmaking blast furnace. *Powder Technol.* **2017**, *314*, 542–549. [CrossRef]

22. Cui, J.; Hou, Q.; Shen, Y. CFD-DEM study of coke combustion in the raceway cavity of an ironmaking blast furnace. *Powder Technol.* **2020**, *362*, 539–549. [CrossRef]

23. Lu, Y.; Liu, S.; Zhang, X.; Jiang, Z.E.D. A Probabilistic Statistical Method for the Determination of Void Morphology with CFD-DEM Approach. *Energies* **2020**, *13*, 4041. [CrossRef]

24. Hilton, J.E.; Cleary, P.W. Raceway formation in laterally gas-driven particle beds. *Chem. Eng. Sci.* **2012**, *80*, 306–316. [CrossRef]

25. Lichtenegger, T.; Pirker, S. CFD-DEM modeling of strongly polydisperse particulate systems. *Powder Technol.* **2018**, *325*, 698–711. [CrossRef]

26. Mondal, S.S.; Som, S.K.; Dash, S.K. Numerical predictions on the influences of the air blast velocity, initial bed porosity and bed height on the shape and size of raceway zone in a blast furnace. *J. Phys. D Appl. Phys.* **2005**, *38*, 1301–1307. [CrossRef]

27. Singh, V.; Gupta, G.S.; Sarkar, S. Study of gas cavity size hysteresis in a packed bed using DEM. *Chem. Eng. Sci.* **2007**, *62*, 6102–6111. [CrossRef]

28. Sun, Y.; Chen, R.; Zhang, Z.; Wu, G.; Zhang, H.; Li, L.; Liu, Y.; Li, X.; Huang, Y. Numerical simulation of the raceway zone in melter gasifier of COREX process. *Processes* **2019**, *7*, 867. [CrossRef]

29. Rangarajan, D.; Shiozawa, T.; Shen, Y.; Curtis, J.S.; Yu, A. Influence of operating parameters on raceway properties in a model blast furnace using a two-fluid model. *Ind. Eng. Chem. Res.* **2014**, *53*, 4983–4990. [CrossRef]

30. Gu, M.; Zhang, M.; Selvarasu, N.K.C.; Zhao, Y.C.Q.Z. Numerical Analysis of Pulverized Coal Combustion inside Tuyere and Raceway. *Steel Res. Int.* **2008**, *79*, 17–24. [CrossRef]

31. Fu, D.; Zheng, D.; Zhou, C.Q.; D'Alessio, J.; Ferron, K.J.; Zhao, Y. Parametric studies on pci performances. ASME/JSME 2011 8th Therm. *Eng. Jt. Conf. AJTEC* **2011**. [CrossRef]

32. Okosun, T.; Street, S.J.; Zhao, J.; Wu, B.; Zhou, C.Q. Influence of conveyance methods for pulverised coal injection in a blast furnace. *Ironmak. Steelmak.* **2017**, *44*, 513–525. [CrossRef]

33. Fu, D.; Tang, G.; Zhao, Y.; D'Alessio, J.; Zhou, C.Q. Integration of Tuyere, Raceway and Shaft Models for Predicting Blast Furnace Process. *JOM* **2018**, *70*, 951–957. [CrossRef]

34. Wu, D.; Zhou, P.; Zhou, C.Q. Evaluation of pulverized coal utilization in a blast furnace by numerical simulation and grey relational analysis. *Appl. Energy* **2019**, *250*, 1686–1695. [CrossRef]

35. Okosun, T.; Silaen, A.K.; Zhou, C.Q. Review on Computational Modeling and Visualization of the Ironmaking Blast Furnace at Purdue University Northwest. *Steel Res. Int.* **2019**, *90*, 1–16. [CrossRef]

36. Zhuo, Y.; Shen, Y. Three-dimensional transient modelling of coal and coke co-combustion in the dynamic raceway of ironmaking blast furnaces. *Appl. Energy* **2020**, *261*, 114456. [CrossRef]

37. Gidaspow, D. *Multiphase Flow and Fluidization: Continuum and Kinetic Theory Descriptions*; Academic Press: New York, NY, USA, 1994; 467p.

38. Ding, J.; Gidaspow, D. A bubbling fluidization model using kinetic theory of granular flow. *AIChE J.* **1990**, *36*, 523–538. [CrossRef]

39. Lun, C.K.K.; Savage, S.B.; Jeffrey, D.J.; Chepurniy, N. Kinetic theories for granular flow: Inelastic particles in Couette flow and slightly inelastic particles in a general flowfield. *J. Fluid Mech.* **1984**, *140*, 223–256. [CrossRef]

40. Schaeffer, D.G. Instability in the evolution equations describing incompressible granular flow. *J. Differ. Equ.* **1987**, *66*, 19–50. [CrossRef]

41. Ocone, R.; Sundaresan, S.; Jackson, R. Gas-Particle flow in a duct of arbitrary inclination with particle-particle interactions. *AIChE J.* **1993**, *39*, 1261–1271. [CrossRef]

42. Johnson, P.C.; Jackson, R. Frictional–collisional constitutive relations for granular materials, with application to plane shearing. *J. Fluid Mech.* **1987**, *176*, 67–93. [CrossRef]